

High Thermoelectric Performance and Defect Energetics of Multipocketed Full-Heusler Compounds

Junsoo Park,^{1,*} Yi Xia,² Alex M. Ganose,¹ Anubhav Jain,^{1,†} and Vidvuds Ozoliņš^{3,4,‡}

¹*Energy Technologies Area, Lawrence Berkeley National Laboratory, Berkeley, CA 94720, USA*

²*Department of Materials Science & Engineering, Northwestern University, Evanston, IL 60208, USA*

³*Department of Applied Physics, Yale University, New Haven, CT 06511, USA*

⁴*Energy Sciences Institute, Yale University, West Haven, CT 06516, USA*

(Dated: August 4, 2020)

We report first-principles density-functional study of electron-phonon interactions and thermoelectric transport properties of full-Heusler compounds Sr₂BiAu and Sr₂SbAu. Our results show that ultrahigh intrinsic bulk thermoelectric performance across a wide range of temperatures is physically possible and point to the presence of multiply degenerate and highly dispersive carrier pockets as the key factor for achieving it. Sr₂BiAu, which features ten energy-aligned low effective mass pockets (six along $\Gamma - X$ and four at L), is predicted to deliver n -type $zT = 0.4 - 4.9$ at $T = 100 - 700$ K. Comparison with the previously investigated Ba₂BiAu compound shows that the additional L -pockets in Sr₂BiAu significantly increase its low-temperature power factor to a maximum value of $12 \text{ mW m}^{-1} \text{ K}^{-2}$ near $T = 300$ K. However, at high temperatures the power factor of Sr₂BiAu drops below that of Ba₂BiAu because the L states are heavier and subject to strong scattering by phonon deformation as opposed to the lighter $\Gamma - X$ states that are limited by polar-optical scattering. Sr₂SbAu is predicted to deliver lower n -type of $zT = 3.4$ at $T = 750$ K due to appreciable misalignment between the L and $\Gamma - X$ carrier pockets, generally heavier scattering, and slightly higher lattice thermal conductivity. Soft acoustic modes, responsible for low lattice thermal conductivity, also increase vibrational entropies and high-temperature stability of the Heusler compounds, suggesting that their experimental synthesis may be feasible. The dominant intrinsic defects are found to be Au vacancies, which drive the Fermi level towards the conduction band and work in favor of n -doping.

I. INTRODUCTION

Thermoelectricity is a clean energy harvesting technology that allows direct interconversion between heat and electric current. The indicator of thermoelectric efficiency is the dimensionless figure of merit known as zT . To date, bulk thermoelectric materials have not overcome $zT = 3$, with $zT = 2$ only achieved in a few chalcogenide compounds [1–10]. Materials that deliver commercially-relevant performance below room temperature are particularly scarce, where alloys of Bi₂Te₃ [11–13] and Mg₃Sb₂-Mg₃Bi₂ [14–17] are essentially the only materials with zT near 1. This is unfortunate since many industrial applications, including refrigeration and spacecraft propulsion, would greatly benefit from efficient thermoelectrics at room-to-cryogenic temperatures [18–21].

The dearth of efficient thermoelectrics especially at low temperatures can easily be inferred from the definition $zT = \frac{\alpha^2 \sigma T}{\kappa}$. Here, $\alpha^2 \sigma$ is the thermoelectric power factor (PF), composed of the Seebeck coefficient (α) and electronic conductivity (σ). The total thermal conductivity (κ) is the sum of lattice thermal conductivity and electronic thermal conductivity ($\kappa_{\text{lat}} + \kappa_{\text{e}}$). A desirable thermoelectric material requires high α and σ with low κ . Unfortunately, such a combination is inherently difficult

to achieve [22–27]. At low temperatures, due to small T and high κ_{lat} , designing for high PF is all the more indispensable, but unfortunately high PF is generally limited by the counterproductive behaviors of α and σ . High σ must then arise from high mobility (μ) since attempts to boost it via doping necessarily suppresses α . A large number of band pockets is generally thought to enhance σ at presumably little to no expense in α because it can deliver higher carrier concentration for given Fermi level. These considerations are best represented by bands of 1) small effective mass (m) capable of producing μ and 2) high band degeneracy or pocket multiplicity [26, 28–32].

As a culmination of these concepts, full-Heusler Ba₂BiAu (n -type) was recently studied based on a rigorous treatment of electron-phonon and phonon-phonon scattering, and has led to the prediction of an unprecedentedly high $zT \approx 5$ at 700 K and a promising $zT \approx 1.5$ at 300 K [33, 34]. In this compound, one highly dispersive conduction band pocket along sixfold degenerate $\Gamma - X$ proved critical to the high PF. Meanwhile, κ_{lat} is minimal due to anharmonic rattling of Au atoms, a trait shared by this class of full-Heusler compounds [35]. The study showcased a rare coexistence of very high PF and ultralow κ_{lat} for bulk thermoelectrics — albeit without consideration of dopability and the experimental realizability of the compound.

In the present work, we achieve the following. 1) We show that analogous but multi-pocketed full-Heusler compounds, in particular Sr₂BiAu, can theoretically attain even higher thermoelectric performance across a

* qkwnstn@gmail.com

† ajain@lbl.gov

‡ vidvuds.ozolins@yale.edu

broader temperature spectrum, which is especially niche at low temperatures. 2) We analyze the benefit of pocket multiplicity in the form of accidental (non-symmetry-related) degeneracy, which is conditional upon the similarities of the pockets. 3) We predict that the Heusler phase stability is entropically favored and that the lowest-energy defect, Au vacancy, is favorable for n -doping.

II. COMPUTATIONAL METHODS

A. Electronic Structures

The electronic structure is calculated with Quantum Espresso [36, 37] with the Optimized Norm-Conserving Vanderbilt pseudopotentials [38–40] and Perdew-Burke-Ernzerhof (PBE) exchange-correlation functional [41] with and without spin-orbit coupling (SOC) for comparisons. Plane-wave cutoff of 100 Ry is used. In order to obtain more accurate band gaps, advanced functionals such as the modified Becke-Johnson potential (mBJ) by Tran and Blaha [42] and the Heyd-Scuseria-Ernzerhof hybrid-exchange functional (HSE06) [43, 44] were used.

B. Electron-phonon Scattering

In treating electron-phonon scattering, we first compute electronic states and e-ph interaction matrix elements at a coarse $8 \times 8 \times 8$ \mathbf{k} -point mesh, using phonon perturbations computed at a coarse $4 \times 4 \times 4$ \mathbf{q} -point mesh using density functional perturbation theory (DFPT) [45, 46]. Then with the EPW package [47–50] we interpolate electronic states, phonons, and the matrix elements onto dense $40 \times 40 \times 40$ \mathbf{k} -point and \mathbf{q} -point meshes through maximally localized Wannier functions [51–53]. Long-ranged polar optical scattering matrix elements are added on the dense \mathbf{k} -mesh [54]. The imaginary part of the resulting electron self-energy leads directly to band-and- \mathbf{k} -dependent electron lifetimes ($\tau_{\nu\mathbf{k}}$) limited by electron-phonon (e-ph) scattering. Further theoretical details can be found in Supplemental Material at [URL will be inserted by publisher] [55].

C. Electron Transport

With $\tau_{\nu\mathbf{k}}$ as inputs, we employ the Boltzmann transport formalism (implemented in BoltzTraP [56] modified in-house) in the relaxation time approximation (RTA) to compute electron transport properties:

$$\sigma = \frac{1}{\Omega N_{\mathbf{k}}} \sum_{\nu\mathbf{k}} (\tau v^2)_{\nu\mathbf{k}} \left(-\frac{\partial f}{\partial E} \right)_{\nu\mathbf{k}}, \quad (1)$$

$$\alpha = \frac{\sigma^{-1}}{\Omega T N_{\mathbf{k}}} \sum_{\nu\mathbf{k}} (\tau v^2)_{\nu\mathbf{k}} (E_{\mathbf{F}} - E_{\nu\mathbf{k}}) \left(-\frac{\partial f}{\partial E} \right)_{\nu\mathbf{k}}, \quad (2)$$

$$\kappa_e = \frac{1}{\Omega T N_{\mathbf{k}}} \sum_{\nu\mathbf{k}} (\tau v^2)_{\nu\mathbf{k}} (E_{\mathbf{F}} - E_{\nu\mathbf{k}})^2 \left(-\frac{\partial f}{\partial E} \right)_{\nu\mathbf{k}} - \alpha^2 \sigma T. \quad (3)$$

The validity of RTA coupled with e-ph matrix elements calculated via DFPT and Wannier interpolation has been well-established by multiple recent instances of application that approximated experimental measurements well [57–60]. In performing Eqs. 1–3 we utilize the band structure calculated with SOC and the band gap value from mBJ+SOC for consistent comparison with our previous study on Ba_2BiAu . For Sr_2BiAu , since the effect of SOC on the electronic structure or phonon is minimal (as will be shown), SOC is neglected for the computations of electron-phonon scattering, due to the computational expense. For Sr_2SbAu , however, SOC substantially impacts the electronic structure and is therefore included in electron-phonon scattering computations.

D. Stability and Defects

We use Vienna *Ab initio* Simulations Package (VASP) [61–64] throughout this section to perform DFT total energy calculations for both competing phases and defective supercells. We also incorporate SOC and use the projector-augmented wave (PAW) pseudopotentials [65] with the PBE functional throughout.

All binary and ternary phases that could potentially form from the compositions of the Heuslers compounds available on Materials Project [66] and Inorganic Crystal Structure Database [67–69] are considered for the evaluation of phase stability. Sr_2BiAu has thirteen competing binary and ternary phases, while Ba_2BiAu has ten, Sr_2SbAu twelve, and Ba_2SbAu fifteen. We construct the ternary phase diagrams using the calculated formation energies (shown in Fig. S4 of Supplemental Material [55]), which reveal the phase fields under each of which various pairs of competing phases may coexist with the compounds of interest. The equilibrium chemical potentials are derived using the corresponding phase fields. Of note, all compounds with energies within the numerical noise of DFT (~ 10 meV per atom) from the convex hull were placed on the hull.

We consider all possible vacancy and antisite intrinsic point defects, and employ the standard supercell approach. We create host and defective supercells that are $2 \times 2 \times 2$ expansions of the fully relaxed conventional cubic unit cells of the compounds. The host supercells contain 128 atoms, of which 64 are Ba/Sr atoms, 32 are Bi/Sb atoms, and 32 are Au atoms. This is allowed for all types of point defects because a full-Heusler crystal structure remains identical upon the exchange of lattice sites between the Ba/Sr atoms and the Bi/Sb and Au atoms. For charged supercells, electrons are either removed or added according to the charge. For total energies of defective supercells, a plane-wave cut-off energy of 600 eV and a $2 \times 2 \times 2$ \mathbf{k} -point mesh are used throughout all self-consistent calculations of defective supercells. All

relaxations are performed with the Methfessel-Paxton's smearing scheme [70] to properly treat the metallic characteristics of the cells with charged defects.

Point defect formation energies are calculated as

$$\Delta E_f^D = E^D - E^{\text{Host}} - \sum_a \Delta N_a \mu_a + q(E_v + E_F) + E_{\text{cor}}, \quad (4)$$

where E^D is the total energy of a defective cell, E^{Host} is the total energy of a host full-Heusler cell into which a defect is introduced, q is the charge on the defect and μ_a is the chemical potential of element a in the compounds (e.g., as determined by the phase diagram). ΔN_a is the excess (positive) or deficient (negative) number of atoms of element a in the defective cell relative to the host cell. For instance, if the defect is Bi_{Au} antisite (Bi in place of Au), then $\Delta N_{\text{Bi}} = 1$ and $\Delta N_{\text{Au}} = -1$. E_F is a free parameter and represents the Fermi level as counted positively up from E_v , which is the energy required to remove an electron from a given host, i.e., the valence band maximum (VBM) of the host compound. Lastly, E_{cor} is a correction term for finite-sized supercells, which experience several fictitious effects.

Charged defects experience fictitious electrostatic interactions between periodic images of the defect, due to periodic boundary condition, and interactions between the defect and the homogeneous, jellium-like background charge that enforces overall charge-neutrality. These are corrected by the method of Makov and Payne [71],

$$E_{\text{cor}} = \frac{q^2 \gamma}{2\epsilon L} - \frac{2\pi q Q}{3\epsilon L^3}, \quad (5)$$

where γ is the Madelung constant, Q is the quadrupole moment, L is the supercell lattice parameter, and ϵ is the dielectric constant of the host compound. While more sophisticated correction schemes have been proposed [72–74], we do not employ them because 1) the compounds have high dielectric constants, 2) cell sizes used are large enough for Eq. 5 to be acceptable ($L > 16 \text{ \AA}$), and 3) other methods will likely not change the main conclusions we draw. Band-gap correction also must be performed to reference the defect energies to more realistic band edges of the host compounds, for which we use HSE06 with SOC. This treatment scheme of choice is based on HSE06's credible track record of preserving the band-edge-relative defect energies calculated with PBE when aligned to a common reference level (achieved with the local electrostatic potential) [75–79]. Potential adjustment as well as band-filling corrections are made [74]. These corrections are computed using the aide code (not yet published). Additional details on calculations of phase stability and defect energies are provided in the Supplementary Material [55].

III. ELECTRONIC PROPERTIES

A. The Electronic Structure

The band structures of Sr_2BiAu and Sr_2SbAu are shown in Fig. 1a–b. Sr_2BiAu and Sr_2SbAu feature additional dispersive conduction band pockets at the fourfold degenerate L -point while retaining the sixfold degenerate pocket along $\Gamma - X$. SOC does not affect the conduction band pocket along $\Gamma - X$, just as in the case of Ba_2BiAu . The corresponding energy surfaces as seen in Fig. 1c reveal all ten pockets. Whereas the L -pocket of Sr_2BiAu is nearly energy-aligned with the $\Gamma - X$ -pocket, the L -pocket of Sr_2SbAu is lower than the $\Gamma - X$ -pocket by 0.06 eV. The effective masses of the very dispersive $\Gamma - X$ -pocket are essentially identical for all three com-

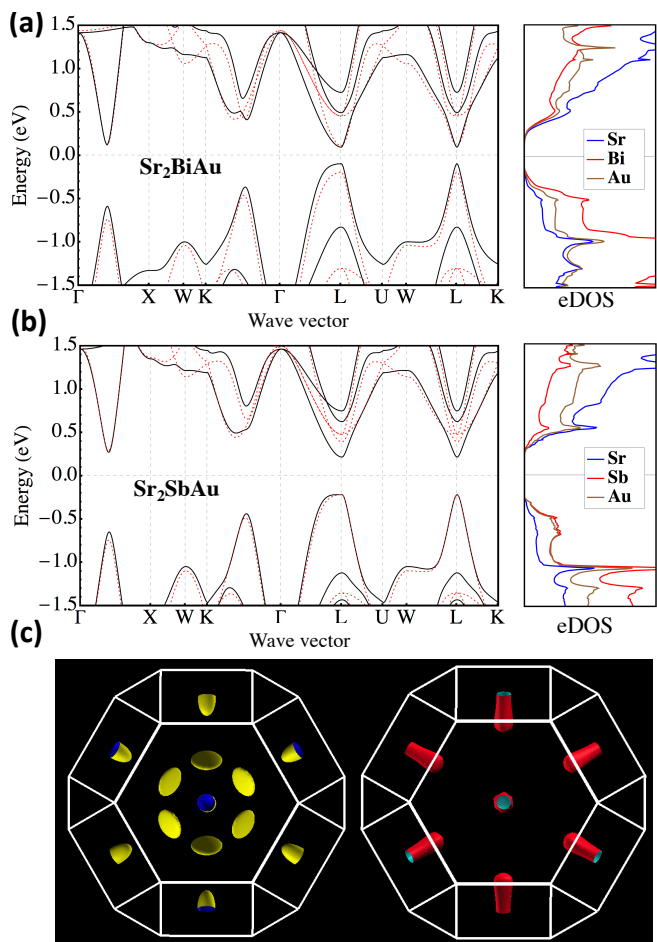


FIG. 1. (Color online) **a)** Electronic band structures of Sr_2BiAu with (black, solid) and without (red, dotted) SOC, aligned at the CBM. The atom-decomposed density of states with SOC is shown on the right. **b)** Same for Sr_2SbAu . **c)** Isoenergy surfaces of Sr_2SbAu with SOC, at 0.1 eV above the CBM (left) and below the VBM (right). The levels correspond to electron doping concentration of $n_e = 1.44 \times 10^{20} \text{ cm}^{-3}$ and hole doping concentration of $n_h = 1.40 \times 10^{20} \text{ cm}^{-3}$, respectively.

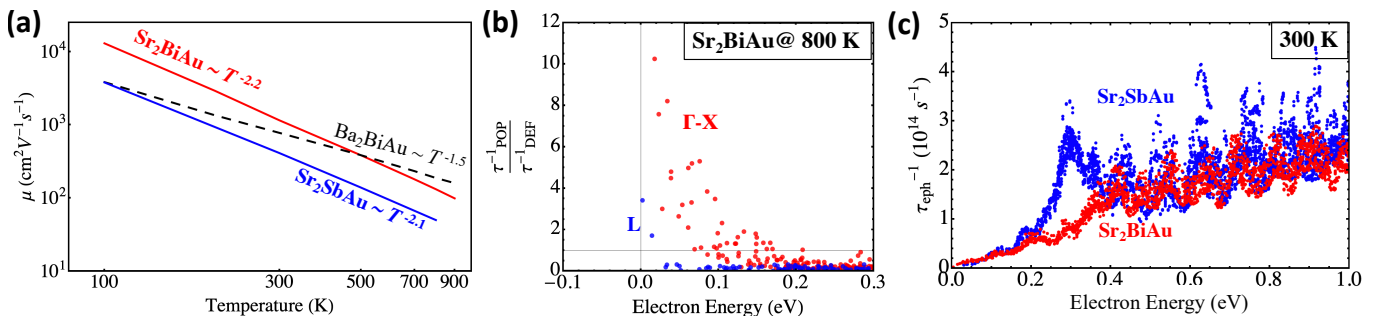


FIG. 2. (Color online) **a**) Comparison of electron mobilities of the Heusler compounds at low and high temperatures. **b**) The relative strength of polar-optical scattering (POP) and lattice deformation scattering (DEF) of the $\Gamma - X$ -pocket (red), which is clearly dominated by POP, and the L -pocket (blue) which is heavily affected by DEF. **c**) Relative e-ph scattering rates of Sr_2BiAu and Sr_2SbAu at 300 K.

pounds at approximately $m_{\parallel} = 0.067$ and $m_{\perp} = 0.48$. The L -pockets are somewhat less dispersive, and their principal effective masses are approximately $m_{\parallel} = 0.19$ and $m_{\perp} = 0.45$ for both of the Sr-compounds.

A popular index for correlating a band structure to the PF it generates is the so-called Fermi surface complexity factor, calculated as [31]

$$C = N_{\text{pocket}} \left(\frac{2}{3} \left(\frac{m_{\perp}}{m_{\parallel}} \right)^{\frac{1}{3}} + \frac{1}{3} \left(\frac{m_{\perp}}{m_{\parallel}} \right)^{-\frac{2}{3}} \right)^{3/2}, \quad (6)$$

The band characters as described above yield complexity factors of 9.5 for Ba_2BiAu , which only has a $\Gamma - X$ -pocket, and 14 for the two Sr-compounds, though the value is ambiguous for Sr_2SbAu where the pockets are misaligned.

The band gaps as calculated by PBE+SOC are 0.19 eV for Sr_2BiAu and 0.5 eV for Sr_2SbAu , which are severe underestimations. The mBJ functional with SOC yields 0.53 eV Sr_2BiAu and 0.85 eV for Sr_2SbAu , where HSE06 with SOC yields 0.53 eV and 0.81 eV, respectively.

B. Scattering & Mobility

Electron mobilities of the three Heusler compounds, calculated using band-and- \mathbf{k} -dependent electron-phonon lifetimes, are juxtaposed in Fig. 2a. Electron mobilities of the two Sr compounds decay at a faster rate with temperature than that of Ba_2BiAu . This is due to the extra pocket L -pocket that the Sr compounds have. The L -pocket is overall heavier than the $\Gamma - X$ -pocket and attains a larger electronic density of states (eDOS). Whereas the $\Gamma - X$ -pocket is dispersive enough that the phase space for lattice deformation scattering is small, allowing polar-optical scattering to dominate, the heavier L -pocket is much more affected by deformation scattering [see Fig. 2c]. It is well known that lattice deformation results in quicker temperature-decay of mobility than polar-optical interactions. Therefore, presence of the L -states result in faster decay of mobility with temperature than if only the $\Gamma - X$ -pocket were present,

which in turn results in quicker decay of mobilities of the Sr compounds than that of Ba_2BiAu .

Though the mobilities of the Sr compounds exhibit similar trends, they notably differ in magnitude. This is partially due to the fact that the heavier L -pocket is the true band minimum in Sr_2SbAu , whereas in Sr_2BiAu it is nearly perfectly aligned with the $\Gamma - X$ -pocket. Sr_2SbAu also generally experiences somewhat heavier scattering especially around 0.3 eV above the CBM, as seen in Fig. 2c. The differences in the temperature-dependence of mobility arising from accidentally degenerate pockets that are disparate in character translate to the behavior of their thermoelectric properties of the compounds, as will be seen.

We find that there is little to no intervalley scattering between the two pockets. When we artificially remove the L -pockets such that their participation to scattering of other states is forbidden, we detect virtually no change in the scattering rates of the remaining $\Gamma - X$ -pocket.

IV. THERMOELECTRIC PROPERTIES

A. The Power Factor

Sr_2BiAu is capable of attaining very high n -type PFs across all temperatures, as shown in Fig. 3a, topping out at $12 \text{ mW m}^{-1}\text{K}^{-2}$ near room temperature. Sr_2SbAu simply performs worse, as made clear by Fig. 3b. It is a well-known engineering strategy to boost the PF to engineer bands of multiple pockets for energy convergence [82, 83]. In essence Sr_2BiAu is a natural realization of this concept. Its theoretical PF limited by e-ph scattering hovers above the measured PF of the p -type NbFeSb [80] across all temperature domains [see Fig. 3c]. In contrast, Sr_2SbAu falls short of such natural band convergence as the heavier L -pocket is lower than the $\Gamma - X$ -pocket by 0.06 eV. This, together with somewhat heavier scattering in Sr_2SbAu , results in both lower σ and α for lower PF in comparison to Sr_2BiAu [see Fig. 3d.]

Comparison of Sr_2BiAu and Ba_2BiAu provides insights

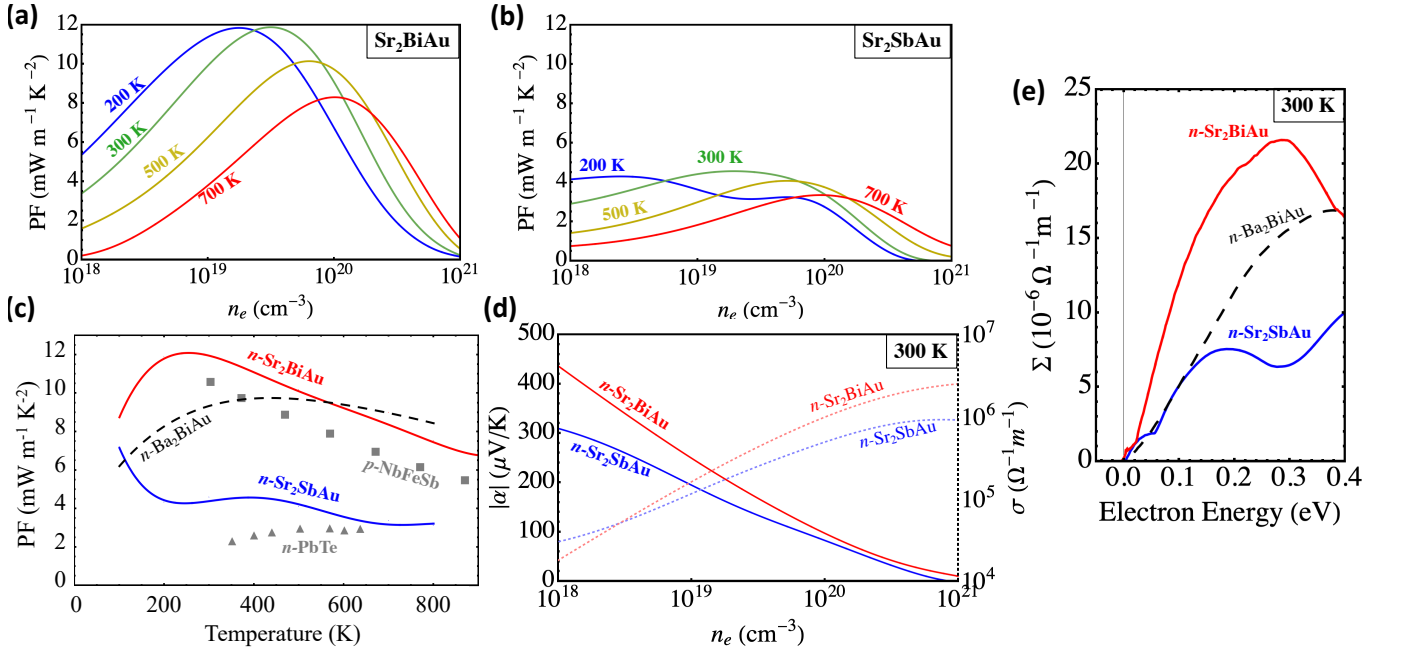


FIG. 3. (Color online) The electron-phonon-scattering-limited n -type power factor of **a)** Sr_2BiAu and **b)** Sr_2SbAu against electron doping concentration. **c)** Maximum n -type power factors of Sr_2BiAu and Sr_2SbAu at each temperature juxtaposed with power factors of high-performing thermoelectrics: p -type NbFeSb [80], n -type PbTe [81], and theoretical n -type Ba_2BiAu [33]). **d)** Comparison of the n -type Seebeck coefficient (solid) and conductivity (dotted) of Sr_2BiAu (red) and Sr_2SbAu (blue) at 300 K. **e)** The spectral conductivities of three full-Heusler compounds at 300 K, where they are all zero-aligned to their respective CBMs.

to the effects of the additional, heavier L -pocket and the aforementioned temperature-dependent mobility profiles. At low temperatures, the PFs behave as expected from the complexity factors, and Sr_2BiAu easily performs better than Ba_2BiAu . However as higher temperatures excite deeper L states whose lifetimes decay more quickly with energy (as reflected by mobilities), Ba_2BiAu begins to outperform Sr_2BiAu . Such a crossover indicates that the additional presence of a heavier pocket, under larger influence of lattice deformation scattering, benefits the PF only below certain threshold temperature past which the deep heavy states with short lifetimes are critically excited, negating the benefit of higher carrier population per Fermi level. The threshold temperature is, in turn, dependent upon the extent to which the second pocket is heavier than the first.

The essence of the overall relationship between the three band structures and their thermoelectric performance is represented by their energy-dependent spectral conductivities, $\Sigma(E) = D(E)\tau(E)v^2(E)$, plotted in Fig. 3e. In comparison to Ba_2BiAu , Sr_2BiAu attains noticeably steeper slope and higher values of $\Sigma(E)$ at its CBM due to simultaneous excitation of the $\Gamma - X$ - and L -pockets. High $\Sigma(E)$ with steep onset is a signature for high PF. Meanwhile, the profile for Sr_2SbAu is kinked: the main incline corresponding to the $\Gamma - X$ -pocket occurs 0.06 eV into the CBM followed by a much more gradual onset corresponding to the heavier L -pocket, and it dips

early around 0.3 eV due to the heavy scattering there. These features are less effective for thermoelectricity.

The main lesson of the above discussions is that a multitude of inherently distinct, symmetry-inequivalent pockets of accidental degeneracy is not necessarily beneficial for thermoelectrics. It better benefits thermoelectric performance if the pockets share similar dispersion and scattering behaviors. If sufficiently different in character, then one may be better off without the heavier pocket as the disparity in pocket lifetimes and mobilities would overpower increased carrier population. Only in the perfectly symmetry-identical cases do more pockets universally lead to higher performance. More generally, this demonstrates that indicators such as the complexity factor are valid in so far as all pockets share similar if not symmetry-identical profiles in not only the band shapes but also scattering behaviors. The complexity factor becomes an increasingly poorer measure of thermoelectric performance as the band pockets are accidentally degenerate and become more disparate in character.

B. Thermal Properties and the Figure of Merit

The Lorenz numbers (L) of the Sr-compounds are consistently below the free-electron Wiedemann-Franz value ($L_{\text{WF}} = 2.44 \times 10^{-8} \text{ W}\Omega\text{K}^{-2}$). $L < L_{\text{WF}}$ by itself is expected as it reflects transport dominated by phonon

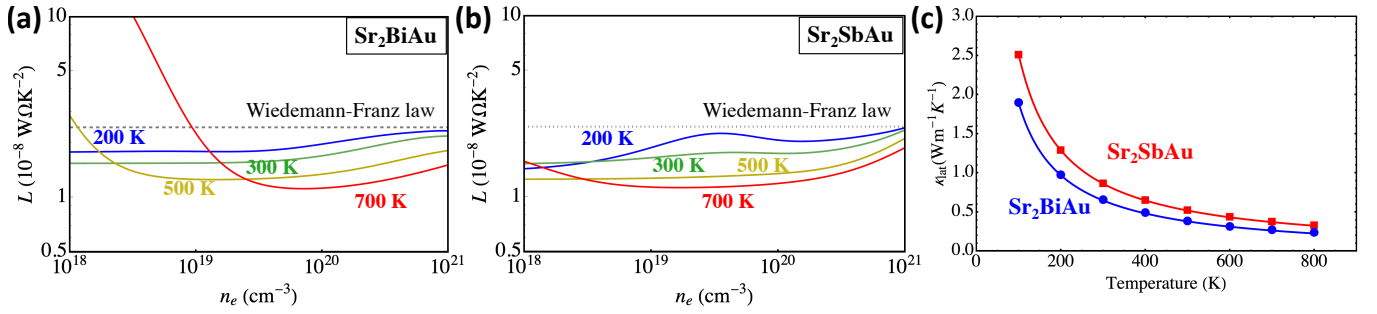


FIG. 4. (Color online) **a)** The Lorenz number of Sr_2BiAu against n -doping concentration. **b)** The Lorenz number of Sr_2SbAu against the Fermi level. The dotted horizontal lines mark the Wiedemann-Franz value. **c)** Lattice thermal conductivities of Sr_2BiAu and Sr_2SbAu .

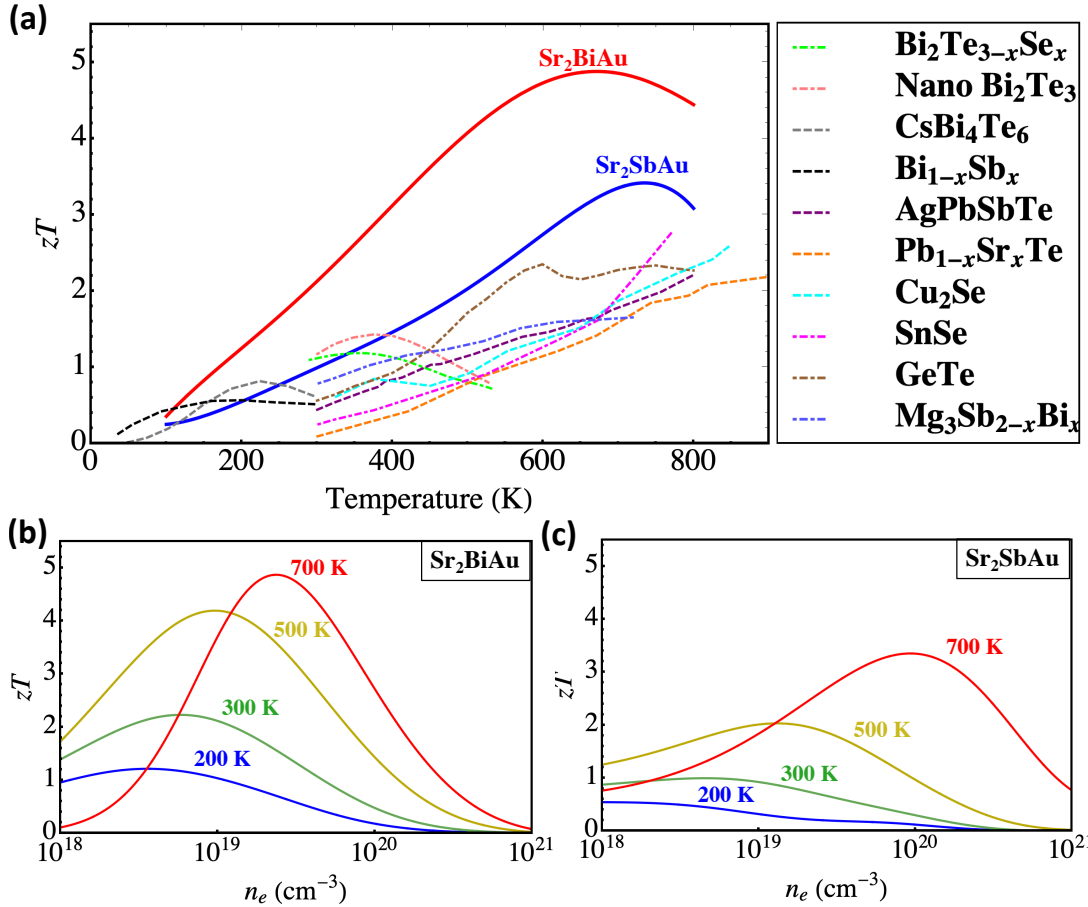


FIG. 5. (Color online) Theoretical n -type zT of **a)** Sr_2BiAu and **b)** Sr_2SbAu against electron doping concentration. **c)** Theoretical *maximum* zT of n -type Sr_2BiAu and Sr_2SbAu at each temperature in comparison to state-of-the-art thermoelectrics [1, 4, 6, 8, 10–13, 15, 16, 84, 85]

scattering, whether due to polar-optical or lattice deformation [86]. Yet upon a closer examination, a couple of anomalies are spotted. L in these two compounds decrease with temperature whereas the free electron picture predicts increasing L (towards L_{WF}) with temperature [86]. Moreover, L reaches as low as $10^{-8} \text{ W}\Omega\text{K}^{-2}$ at high temperatures for the two compounds. We attribute these results to the rapid rate at which scattering rates increase

as the dominant process shifts from polar-optical near the band edge to lattice deformation in the deep electronic states. Referring back to Fig. 3e, about $0.3 \sim 0.35 \text{ eV}$ above the CBMs, $\Sigma(E)$ drops in magnitude after a peak, which is associated with the spike in the scattering rate and eDOS there. High-energy electrons occupying deep states contribute much more to κ_e whereas low-energy electrons contribute more to σ . Therefore, compara-

tively faster decay of lifetimes at high energies, which are increasingly excited at higher temperatures, leads to lower L than if just one scattering mechanism prevailed throughout.

The small magnitudes of L and therefore κ_e relative to σ are particularly important because $\kappa_e > \kappa_{\text{lat}}$ in these compounds. The ultralow κ_{lat} has been predicted by a previous study [35], whose results we reproduce here in Fig. 4c using the same computational methods combining compressive sensing lattice dynamics [87] and iterative Boltzmann transport [88]. Phonon dispersion and density of states can be found in the Supplemental Material [55].

The combination of high PF, and low κ_{lat} and L result in very high intrinsic zT from cryogenic to high temperatures, especially for Sr_2BiAu . Notable in particular is the high performance $zT = 0.4\text{--}2.2$ in the 100–300 K range, which if realized would fill a niche at low temperatures. Comparisons made in Fig. 5a reveal that the theoretical performance of Sr_2BiAu , optimal doping assumed, is record-high at nearly all temperatures for bulk materials. Though not quite as glamorous, Sr_2SbAu is still poised to offer higher zT than most of state-of-the-art thermoelectric compounds. If the offset $\Gamma - X$ -and- L -pockets could be made to align in energy via doping or temperature effect, it would attain even higher PF and zT . Overall, because κ_e is the dominant thermal conductivity and L is rather constant, zT tends to peak at lower E_F (n_e) than the PF where higher Seebeck coefficient develops. This in turn reduces n -doping requirement to achieve optimum performance.

V. STABILITY, DEFECTS, AND DOPABILITY

For the Heusler compounds hereby studied to experimentally realize their thermoelectric potentials, they ought to have a large region of stability and be n -dopable – desirably to their ideal carrier concentrations of $n_e \approx 10^{19} \text{ cm}^{-3}$. With the rapid emergence of computationally discovered hypothetical materials, it is important that analyses of realizability accompany performance predictions for a better guidance to experimentalists [89]. Accordingly we analyze the stability and intrinsic defect energetics of the four full-Heusler compounds (Ba_2SbAu in addition to the three compounds studied above).

A. Phase Stability

We find that the two Bi-compounds, Sr_2BiAu and Ba_2BiAu , are barely thermodynamically stable, as in that they have extremely limited chemical potential spaces of phase stability – essentially single points. Their points of stability are $\mu_{\text{Sr}} \approx -2.66 \text{ eV}$, $\mu_{\text{Bi}} \approx -5.26 \text{ eV}$, and $\mu_{\text{Au}} \approx -4.13$ for Sr_2BiAu , and $\mu_{\text{Ba}} \approx -2.78 \text{ eV}$, $\mu_{\text{Bi}} \approx -5.71 \text{ eV}$, and $\mu_{\text{Au}} \approx -4.25$ for Ba_2BiAu . This is a

rather unfavorable sign for their synthesis. On the other hand, the two Sb-compounds, Sr_2SbAu and Ba_2SbAu , are found to have sizable regions of phase stability as shown in Fig. 6, and therefore are better poised to be synthesized experimentally. It is also worth mentioning that a $P6_3mmc$ phase of 1:1:1 stoichiometry have been experimentally observed [90], which may serve as a starting point for tuning the chemical potentials.

The two Sr-compounds, Sr_2BiAu and Sr_2SbAu , each have a stoichiometrically identical polymorphs of the $P21/m$ phase, as brought up by a previous work [35]. As per our PBE+SOC total energy calculation, these phases are slightly lower in energy than the Heusler counterparts, by approximately 4 meV and 10 meV per atom respectively. However, these small differences are beyond the numerical resolution of DFT, and either polymorph would have a chance of forming. At finite temperatures, the relative stability would thus likely boil down to the entropic contributions to the free energy. We find that the Heusler phases have much higher vibrational entropies (S_v) than the $P21/m$ phases, by $+0.42 k_B$ per atom for Sr_2BiAu and $+0.36 k_B$ per atom for Sr_2SbAu . Fig. 7 shows that the prominently soft acoustic modes of

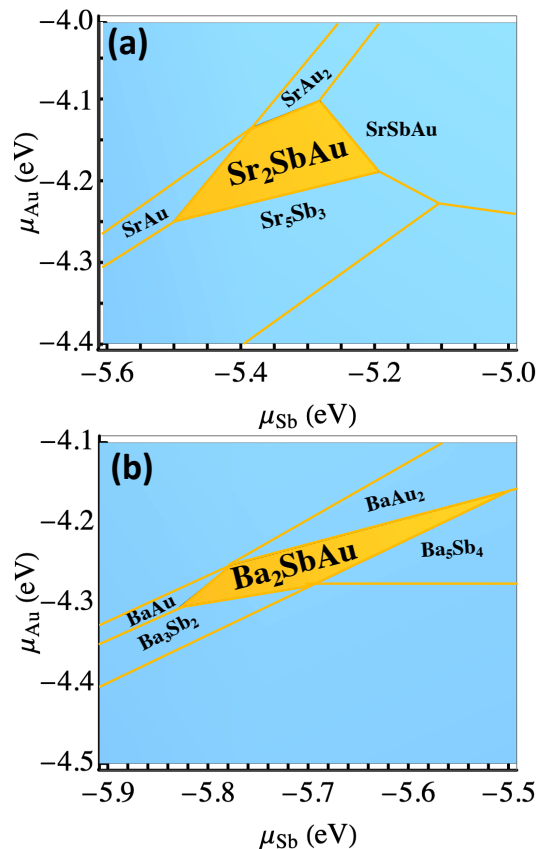


FIG. 6. (Color online) The region of phase stability (shaded orange) of a) Sr_2SbAu and b) Ba_2SbAu in the chemical potential space of Sb (the horizontal axes), and Au (the vertical axes). Secondary competing phases to be found in the vicinity are labeled.

the Heusler phases, represented by the much higher net phonon DOS ($\Delta D(\omega)$) in the low-frequency region, drive their higher S_v . At 300 K, the net gain in ΔS_v of the Heusler phases lowers their free energy of formation by 12 meV and 9 meV per atom, respectively, relative to the $P21/m$ phases. As a result at 300 K, Heusler Sr_2BiAu becomes stable by 8 meV per atom and Heusler Sr_2SbAu also turns essentially stable.

B. Defects

In all four compounds, the lowest-energy defect is Au vacancy (Vac_{Au}). This likely reflects that, at their sites, Au atoms are very weakly bonded in both compounds. It has been discussed in Ref. 35 that due to its filled $5d$ and $6s$ shells, loosely bonded Au atoms act as rattlers with strongly anharmonic vibrations and are key contributors to phonon scattering and very low κ_{lat} in the two compounds. The formation energies are shown in Fig. 8 along with those of the next-highest-energy defects, namely the Au_{Bi} and Bi_{Au} antisites. The small magnitudes of the correction term E_{cor} (less than 0.1 eV for most charged defects for all types) reflect that high ϵ of the compounds inhibit strong electrostatic interactions between charged defects and their periodic images, validating the overall size-sufficiency of the supercells used.

We obtain the defect-limited Fermi levels by enforcing charge neutrality of all defects. Zero-referenced to

the VBMs, the values are 0.62 eV, 0.35 eV, 0.69 eV, and 0.91 eV respectively for Ba_2BiAu , Sr_2BiAu , Sr_2SbAu , and Ba_2SbAu . As these are in all four cases close to the conduction band edges (0.82 eV, 0.42 eV, 0.80 eV, 0.95 eV, respectively), Vac_{Au} intrinsically drives the Heusler systems to be somewhat n -type. However, these defect-pinned Fermi levels correspond to excess electron concentrations of only $10^{15} \sim 10^{18} \text{ cm}^{-3}$ at 300 K [see Fig. S5 in Supplemental Material [55]]. This is not quite sufficient for reaching the optimal doping concentrations of $10^{18} \sim 10^{20} \text{ cm}^{-3}$. Further excess electrons then must be introduced externally. We find that Hg_{Au} , a potent external n -dopant, is stable by more than 100 meV per atom with respect to the convex hull of all other known stable phases formed by the host atoms and Hg. Considering also that Hg is just as heavy as Au, its introduction is expected to preserve the Au-dominated soft acoustic phonons, thus maintaining high positive S_v and low κ_{lat} . For these reasons, toxicity notwithstanding, Hg_{Au} would be a strategic doping mechanism for optimal triggering of n -type performance.

VI. CONCLUSION

In summary, the full-Heuslers in this study - especially Sr_2BiAu - constitute a theoretical validation that very high *intrinsic* thermoelectric performance across a broad range of temperatures from 100 \sim 800 K is physically possible in real bulk compounds. The predicted zT values are notably high at cryogenic-to-room temperatures - the domain that generally lacks efficient thermoelectric materials. Dispersive conduction band pockets at two off-symmetry points (for a total of ten pockets in the Brillouin zone) generate very high power factors across all temperatures. Notably, due to the disparity in the characters of the two pockets in terms of dispersion and dominant scattering mechanisms, the power factor decays more quickly with temperature. Whether accidentally degenerate pockets benefit thermoelectric performance is therefore conditional upon the similarity of the pockets and temperature of operation. If the pockets are too dissimilar, then performance would benefit if the lighter pocket were alone without the heavier pocket.

Fortunately, intrinsic defect energetics is favorable for n -doping. Au vacancy has the lowest formation energy of all defects: 0.2 \sim 0.4 eV for charge-neutral vacancy. All things considered, the two Sb-compounds, Sr_2SbAu and Ba_2SbAu , have the best chance at realization since they have the largest chemical potential regions of phase stability. With the help of external n -dopants such as Hg_{Au} , near-optimal triggering of their thermoelectricity may well be within experimental reach. The Bi-compounds, Sr_2BiAu and Ba_2BiAu , appear to be fundamentally hampered by their constricted stability conditions. Yet, at high temperatures where the effects of vibrational entropy increasingly favors formation of the Heusler phases over others, their realization may stand a better chance.

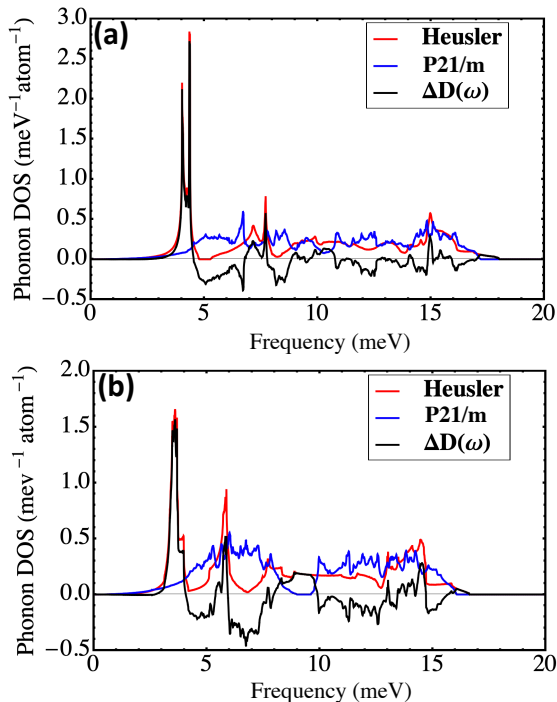


FIG. 7. (Color online) The phonon DOS of the Heusler and $P21/m$ phases and their differences for a) Sr_2SbAu and b) Sr_2BiAu .

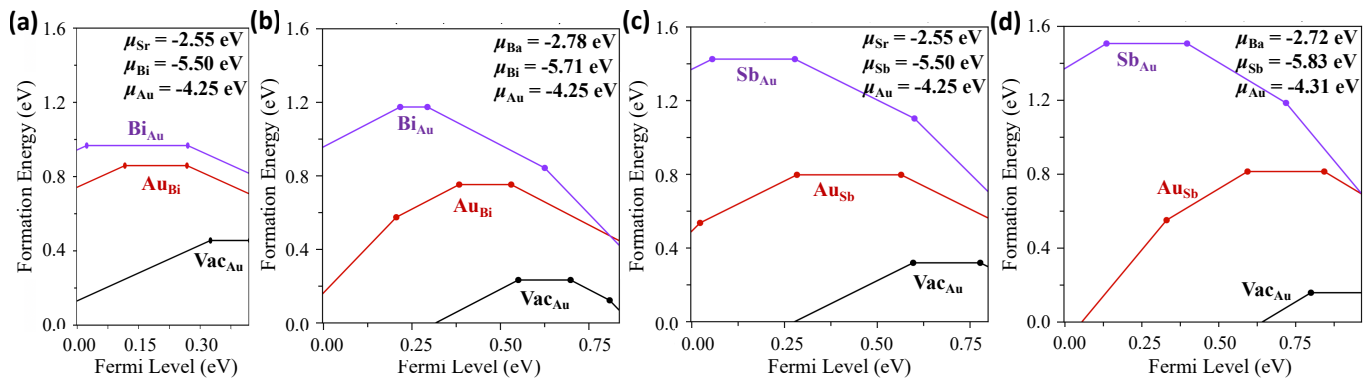


FIG. 8. (Color online) The formation energies of three lowest-energy defects Vac_{Au} , $\text{Au}_{\text{Bi/Sb}}$, and Bi/Sb_{Au} , in **a)** Sr_2BiAu , **b)** Ba_2BiAu , **c)** Sr_2SbAu , and **d)** Ba_2SbAu . The slopes of the lines indicate charge ($q = -2 \sim +2$). The plots go from the VBM (0 eV) to the CBM as determined by HSE+SOC. The chemical potentials for the plots shown correspond to the Au-poor conditions, where μ_{Au} is the lowest, at which Vac_{Au} formation energy is minimized.

ACKNOWLEDGMENTS

The study was conceived and designed on National Science Foundation (NSF) Grant DMR-1611507, which funded V.O. The study was further developed and completed on the grant from U.S. Department of Energy, Office of Basic Energy Sciences, Early Career Research Program, which funded J. P., A. G., and A. J. This research used computational resources of 1) the National Energy

Research Scientific Computing Center (NERSC), a DOE Office of Science User Facility supported by the Office of Science of the U.S. Department of Energy under Contract No. DE-AC02-05CH11231, and 2) Texas Advanced Computing Center (TACC) at the University of Texas at Austin through the Extreme Science and Engineering Discovery Environment (XSEDE), which is supported by NSF grant number ACI-1548562.

- [1] A. A. Olvera, N. A. Moroz, P. Sahoo, P. Ren, T. P. Bailey, A. A. Page, C. Uher, and P. F. P. Poudeu, Partial indium solubility induces chemical stability and colossal thermoelectric figure of merit in Cu_2Se , *Energy Environ. Sci.* **10**, 1668–1676 (2017).
- [2] Bin Zhong, Yong Zhang, Weiqian Li, Zhenrui Chen, Jingying Cui, Wei Li, Yuandong Xie, Qing Hao, and Qinyu He, High superionic conduction arising from aligned large lamellae and large figure of merit in bulk $\text{Cu}_{1.94}\text{Al}_{0.02}\text{Se}$, *Appl. Phys. Lett.* **105**, 123902 (2014).
- [3] L. Zhao, G. Tan, S. Hao, J. He, Y. Pei, H. Chi, H. Wang, S. Gong, H. Xu, V. Dravid, C. Uher, G. J. Snyder, C. Wolverton, and M. G. Kanatzidis, Ultrahigh power factor and thermoelectric performance in hole-doped single-crystal SnSe , *Science* **351**, 141–144 (2016).
- [4] Cheng Chang, Minghui Wu, Dongsheng He, Yanling Pei, Chao-Feng Wu, Xuefeng Wu, Hulei Yu, Fangyuan Zhu, Kedong Wang, Yue Chen, Li Huang, Jing-Feng Li, Jiaqing He, and Li-Dong Zhao, 3D charge and 2D phonon transports leading to high out-of-plane ZT in n -type SnSe crystals, *Science* **360**, 778–783 (2018).
- [5] Anh Tuan Duong, Van Quang Nguyen, Ganbat Duvjir, Van Thiet Duong, Suyong Kwon, Jae Yong Song, Jae Ki Lee, Ji Eun Lee, SuDong Park, Taewon Min, Jaekwang Lee, Jungdae Kim, and Sunglae Cho, Achieving $zT = 2.2$ with Bi-doped n -type SnSe single crystals, *Nat. Commun.* **7** (2016).
- [6] Kuei Fang Hsu, Sim Loo, Fu Guo, Wei Chen, Jeffrey S. Dyck, Ctirad Uher, Tim Hogan, E. K. Polychroniadis, and Mercuri G. Kanatzidis, Cubic $\text{AgPb}_m\text{SbTe}_{2+m}$: Bulk Thermoelectric Materials with High Figure of Merit, *Science* **303**, 818–821 (2004).
- [7] H. J. Wu, L-D Zhao, F.S. Zheng, D. Wu, Y.L. Pei, X. Tong, M.G. Kanatzidis, and J. Q. He, Broad temperature plateau for thermoelectric figure of merit $ZT > 2$ in phase-separated $\text{PbTe}_{0.7}\text{S}_{0.3}$, *Nat. Commun.* **5**, 1–7 (2014).
- [8] Min Hong, Zhi-Gang Chen, Lei Yang, Yi-Chao Zou, Matthew S. Dargusch, Hao Wang, and Jin Zou, Realizing zT of 2.3 in $\text{Ge}_{1-x-y}\text{Sb}_x\text{In}_y\text{Te}$ via Reducing the Phase-Transition Temperature and Introducing Resonant Energy Doping, *Adv. Mater.* **30**, 1705942 (2018).
- [9] Di Wu, Lin Xie, Xiao Xu, and Jiaqing He, High Thermoelectric Performance Achieved in $\text{GeTe?Bi}_2\text{Te}_3$ Pseudo-Binary via Van der Waals Gap-Induced Hierarchical Ferroelectric Domain Structure, *Adv. Funct. Mater.* **18**, 1806613 (2019).
- [10] Juan Li, Xinyue Zhang, Zhiwei Chen, Siqi Lin, Wen Li, Jiahong Shen, Ian T. Witting, Alireza Faghaninia, Yue Chen, Anubhav Jain, Lidong Chen, G. Jeffrey Snyder, and Yanzhong Pei, Low-Symmetry Rhombohedral GeTe Thermoelectrics, *Joule* **2**, 976–987 (2018).
- [11] B. Poudel, Q. Hao, Y. Ma, Y. Lan, A. Minnich, B. Yu, X. Yang, D. Wang, A. Muto, D. Vashaee, X. Chen, J. Liu, M. Dresselhaus, G. Chen, and Z. Ren, High-Thermoelectric Performance of Nanostructured Bismuth Antimony Telluride Bulk Alloys, *Science* **320**, 634–638 (2008).

- [12] Sang Il Kim, Kyu Hyoung Lee, Hyeon A Mun, Hyun Sik Kim, Sung Woo Hwang, Jong Wook Roh, Dae Jin Yang, Weon Ho Shin, Xiang Shu Li, Young Hee Lee, G. Jeffrey Snyder, and Sung Wng Kim, Dense dislocation arrays embedded in grain boundaries for high-performance bulk thermoelectrics, *Science* **348**, 109–114 (2015).
- [13] L. Hu, H. Wu, T. Zhu, C. Fu, J. He, P. Ying, and X. Zhao, Tuning multiscale microstructures to enhance thermoelectric performance of n -type bismuth-telluride-based solid solutions, *Adv. Energy Mater.* **5**, 1500411 (2015).
- [14] Jiawei Zhang, Lirong Song, Steffen Hindborg Pedersen, Hao Yin, Le Thanh Hung, and Bo Brummerstedt Iversen, Discovery of high-performance low-cost n -type Mg_3Sb_2 -based thermoelectric materials with multi-valley conduction bands, *Nat. Commun.* **8** (2017).
- [15] Maxwell Wood, Jimmy Jiahong Kuo, Kazuki Imasato, and Gerald Jeffrey Snyder, Improvement of Low-Temperature zT in a $\text{Mg}_3\text{Sb}_2/\text{Mg}_3\text{Bi}_2$ Solid Solution via Mg-Vapor Annealing, *Adv. Mater.* **31** (2019).
- [16] Xuemin Shi, Cheng Sun, Zhonglin Bu, Xinyue Zhang, Yixuan Wu, Siqi Lin, Wen Li, Alireza Faghaninia, Anubhav Jain, and Yanzhong Pei, Revelation of Inherently High Mobility Enables Mg_3Sb_2 as a Sustainable Alternative to n - Bi_2Te_3 Thermoelectrics, *Adv. Sci.* **6** (2019).
- [17] Jun Mao, Hangtian Zhu, Zhiwei Ding, Zihang Liu, Geethal Amila, Gamage, Gang Chen, and Zhifeng Ren, High thermoelectric cooling performance of n -type Mg_3Bi_2 -based materials, *Science* **365** (2019).
- [18] Lon E. Bell, Cooling, Heating, Generating Power, and Recovering Waste Heat with Thermoelectric Systems, *Science* **321**, 1457–1461 (2008).
- [19] Jian He and Terry M. Tritt, Advances in Thermoelectric Materials Research: Looking back and moving forward, *Science* **357**, 1–9 (2017).
- [20] T.M. Tritt and M.A. Subramanian, Thermoelectric materials, phenomena, and applications: a birds eye view, *MRS Bulletin* **31**, 188–198 (2006).
- [21] J. Yang and T. Caillat, Thermoelectric materials for space and automotive power generation, *MRS Bulletin* **31**, 224–229 (2006).
- [22] J. Snyder and E. Toberer, Complex thermoelectric materials, *Nat. Mater.* **7**, 105–114 (2008).
- [23] J. R. Sootsman, D. Chung, and M.G. Kanatzidis, New and old concepts in thermoelectric materials, *Angew. Chem.* **48**, 8616–8639 (2009).
- [24] W. G. Zeier, A. Zevalkink, Z. M. Gibbs, G. Hautier, M. G. Kanatzidis, and G. J. Snyder, Thinking Like a Chemist: Intuition in Thermoelectric Materials, *Angew. Chem.* **55**, 6826–6841 (2016).
- [25] Li-Dong Zhao Xiao Zhang, Thermoelectric materials: Energy conversion between heat and electricity, *J. Materiomics.* **1**, 92–105 (2015).
- [26] T. Zhu, Y. Liu, C. Fu, J. P. Heremans, J. G. Snyder, and X. Zhao, Compromise and Synergy in High-Efficiency Thermoelectric Materials, *Adv. Mater.* **29**, 1605884 (2017).
- [27] Jun Mao, Zihang Liu, Jiawei Zhou, Hangtian Zhu, Qian Zhang, Gang Chen, and Zhifeng Ren, Advances in Thermoelectrics, *Adv. in Phys.* **67**, 69–147 (2018).
- [28] Yanzhong Pei, Aaron D. LaLonde, Heng Wang, and G. Jeffrey Snyder, Low Effective Mass Leading to High Thermoelectric Performance, *Energy Environ. Sci.* **5**, 7963–7969 (2012).
- [29] Prashun Gorai, Vladan Stevanović, and Eric S. Toberer, Computationally guided discovery of thermoelectric materials, *Nat. Rev. Mater.* **2**, 1–16 (2017).
- [30] Chenguang Fu, Tiejun Zhu, Yanzhong Pei, Hanhui Xie, Heng Wang, G. Jeffrey Snyder, Yong Liu, Yintu Liu, and Xinbing Zhao, High Band Degeneracy Contributes to High Thermoelectric Performance in p -Type Half-Heusler Compounds, *Adv. Energy Mater.* **4**, 1400600 (2014).
- [31] Zachary M. Gibbs, Francesco Ricci, Guodong Li, Hong Zhu, Kristin Persson, Gerbrand Ceder, Geoffroy Hautier, Anubhav Jain, and G. Jeffrey Snyder, Effective mass and Fermi surface complexity factor from ab initio band structure calculations, *Comput. Mater.* **3**, 1–7 (2017).
- [32] Jun Yan, Prashun Gorai, Brenden Ortiz, Sam Miller, Scott A. Barnett, Thomas Mason, Vladan Stevanović, and Eric S. Toberer, Material descriptors for predicting thermoelectric performance, *Energy Environ. Sci.* **8**, 983–994 (2015).
- [33] Junsoo Park, Yi Xia, and Vidvuds Ozoliņš, High Thermoelectric Power Factor and Efficiency from a Highly Dispersive Band in Ba_2BiAu , *Phys. Rev. Appl.* **11**, 014058 (2019).
- [34] Jinlong Ma, Arun S. Nissimagoudar, Shudong Wang, and Wu Li, High Thermoelectric Figure of Merit of Full-Heusler Ba_2AuX ($X = \text{As}, \text{Sb}, \text{and Bi}$), *Phys. Status Solidi RRL* **14**, 2000084 (2020).
- [35] J. He, M. Amsler, Y. Xia, S. S. Naghavi, V. Hegde, S. Hao, S. Goedecker, V. Ozoliņš, and C. Wolverton, Ultralow Thermal Conductivity in Full Heusler Semiconductors, *Phys. Rev. Lett.* **117**, 046602 (2016).
- [36] Paolo Giannozzi, Stefano Baroni, Nicola Bonini, Matteo Calandra, Roberto Car, Carlo Cavazzoni, Davide Ceresoli, Guido L Chiarotti, Matteo Cococcioni, Ismaila Dabo, Andrea Dal Corso, Stefano de Gironcoli, Stefano Fabris, Guido Fratesi, Ralph Gebauer, Uwe Gerstmann, Christos Gougoussis, Anton Kokalj, Michele Lazzeri, Layla Martin-Samos, Nicola Marzari, Francesco Mauri, Riccardo Mazzarello, Stefano Paolini, Alfredo Pasquarello, Lorenzo Paulatto, Carlo Sbraccia, Sandro Scandolo, Gabriele Scaluzero, Ari P Seitsonen, Alexander Smogunov, Paolo Umari, and Renata M Wentzcovitch, QUANTUM ESPRESSO: a modular and open-source software project for quantum simulations of materials, *J. Phys. Condens. Matter* , 395502 (19pp) (2009).
- [37] P. Giannozzi, O. Andreussi, T. Brumme, O. Bunau, M Buongiorno Nardelli, M Calandra, R. Car, C. Cavazzoni, D. Ceresoli, and M. Cococcioni, Advanced capabilities for materials modeling with Quantum ESPRESSO, *J. Phys. Condens. Matter* , 465901 (31pp) (2017).
- [38] D. R. Hamann, Optimized norm-conserving Vanderbilt pseudopotentials, *Phys. Rev. B* **88**, 085117 (2013).
- [39] Martin Schlipf and François Gygi, Optimization algorithm for the generation of {ONCV} pseudopotentials, *Comput. Phys. Commun.* **196**, 36–44 (2015).
- [40] Peter Scherpel abd Marco Govoni, Ikutaro Hamada, and Giulia Galli, Implementation and Validation of Fully Relativistic GW Calculations: Spin?Orbit Coupling in Molecules, Nanocrystals, and Solids, *J. Chem. Theory Comput.* **12**, 3523–3544 (2016).
- [41] John P. Perdew, Kieron Burke, and Matthias Ernzerhof, Generalized gradient approximation made simple, *Phys. Rev. Lett.* **77**, 3865–3868 (1996).
- [42] Fabien Tran and Peter Blaha, Accurate Band Gaps of Semiconductors and Insulators with a Semilocal

- Exchange-Correlation Potential, Phys. Rev. Lett. **102**, 226401 (2009).
- [43] Jochen Heyd, Gustavo E. Scuseria, and Matthias Ernzerhof, Hybrid functionals based on a screened Coulomb potential, J. Chem. Phys. **118**, 8207–8215 (2003).
- [44] Jochen Heyd, Gustavo E. Scuseria, and Matthias Ernzerhof, Efficient hybrid density functional calculations in solids: Assessment of the Heyd–Scuseria–Ernzerhof screened Coulomb hybrid functional, J. Chem. Phys. **121**, 1187–1192 (2004).
- [45] S. Poncé, G. Antonius, Y. Gillet, P. Boulanger, J. Laflamme Janssen, A. Marini, M. Côté, and X. Gonze, Temperature dependence of electronic eigenenergies in the adiabatic harmonic approximation, Phys. Rev. B **90**, 214304 (2014).
- [46] S. Poncé, Y. Gillet, J. Laflamme Janssen, A. Marini, M. Verstraete, and X. Gonze, Temperature dependence of the electronic structure of semiconductors and insulators, J. Chem. Phys. **143**, 1028137 (2015).
- [47] Feliciano Giustino, Marvin L. Cohen, and Steven G. Louie, Electron-phonon interaction using Wannier functions, Phys. Rev. B **76**, 165108 (2007).
- [48] Jesse Noffsinger, Feliciano Giustino, Brad D. Malone, Cheol Hwan Park, Steven G. Louie, and Marvin L. Cohen, EPW: A program for calculating the electron-phonon coupling using maximally localized Wannier functions, Comput. Phys. Commun. **55**, 2140–2148 (2010).
- [49] S. Ponce, E. R. Margine, C. Verdi, and F. Giustino, EPW: Electron-phonon coupling, transport and superconducting properties using maximally localized Wannier functions, Comput. Phys. Commun. **55**, 116–133 (2016).
- [50] Feliciano Giustino, Electron-phonon interactions from first principles, Rev. Mod. Phys. **89**, 015003 (2017).
- [51] Nicola Marzari and David Vanderbilt, Maximally localized generalized Wannier functions for composite energy bands, Phys. Rev. B **56**, 12847–12865 (1997).
- [52] Ivo Souza, Nicola Marzari, and David Vanderbilt, Maximally localized Wannier functions for entangled energy bands, Phys. Rev. B **65**, 035109–1–13 (2001).
- [53] Arash A. Mostofi, Jonathan R. Yates, Young-Su Lee, Ivo Souza, David Vanderbilt, and Nicola Marzari, wannier90: A tool for obtaining maximally-localised Wannier functions, Comput. Phys. Commun. **178**, 685–699 (2008).
- [54] C. Verdi and F. Giustino, Fröhlich Electron-Phonon Vertex from First Principles, Phys. Rev. Lett. **115**, 176401 (2015).
- [55] Supplementary materials to the main text for computational details on electron-phonon scattering, phase stability and defects.
- [56] Georg K.H. Madsen and David J. Singh, BoltzTraP. A code for calculating band-structure dependent quantities, Comput. Phys. Commun. **175**, 67–71 (2006).
- [57] Qichen Song, Te-Huan Liu, Jiawei Zhou, Zhiwei Ding, and Gang Chen, *Ab initio* study of electron mean free paths and thermoelectric properties of lead telluride, Mater. Today Phys. **2**, 69–77 (2017).
- [58] Jiang Cao, José D. Querales-Flores, Aoife R. Murphy, Stephen Fahy, and Ivana Savić, Dominant electron-phonon scattering mechanisms in *n*-type PbTe from first principles, Phys. Rev. B **98**, 205202 (2018).
- [59] J. Zhou, H. Zhu, T. Liu, Q. Song, R. He, J. Mao, Z. Liu, W. Ren, B. Liao, D. J. Singh, and G. Chen, Large thermoelectric power factor from crystal symmetry-protected non-bonding orbital in half-Heuslers Nb_{1-x}Ti_xFeSb, Nat. Commun. **9**, 1–9 (2018).
- [60] Yi Xia, Junsoo Park, Fei Zhou, and Vidivuds Ozoliņš, High Thermoelectric Power Factor in Intermetallic CoSi Arising from Energy Filtering of Electrons by Phonon Scattering, Phys. Rev. Appl. **11**, 024017 (2019).
- [61] G. Kresse and J. Hafner, *Ab initio* molecular dynamics for liquid metals, Phys. Rev. B **47**, 558–561 (1993).
- [62] G. Kresse and J. Hafner, *Ab initio* molecular-dynamics simulation of the liquid-metal–amorphous-semiconductor transition in germanium, Phys. Rev. B **49**, 14251–14269 (1994).
- [63] G. Kresse and J. Furthmüller, Efficiency of *ab-initio* total energy calculations for metals and semiconductors using a plane-wave basis set, Comput. Mater. Sci. **6**, 15–50 (1996).
- [64] G. Kresse and J. Furthmüller, Efficient iterative schemes for *ab initio* total-energy calculations using a plane-wave basis set, Phys. Rev. B **54**, 11169–11186 (1996).
- [65] P. E. Blöchl, Projector augmented-wave method, Phys. Rev. B **50**, 17953–17979 (1994).
- [66] A. Jain, S. P. Ong, G. Hautier, W. Chen, W. D. Richards, S. Dacek, S. Cholia, D. Gunter, D. Skinner, G. Ceder, and K. A. Persson, Commentary: The Materials Project: A materials genome approach to accelerating materials innovation, APL Mater. **1**, 1002 (2013).
- [67] G. Bergerhoff and I. D. Brown, Inorganic crystal structure database, Crystallographic Databases, 77–95 (1987).
- [68] Alex Belsky, Mariette Hellenbrandt, Vicky Lynn Karen, and Peter Luksch, New developments in the Inorganic Crystal Structure Database (ICSD): accessibility in support of materials research and design, Acta Crystallogr. B **58**, 364–369 (2002).
- [69] Mariette Hellenbrandt, The Inorganic Crystal Structure Database (ICSD) – Present and Future, Crystallogr. Rev. **10**, 17–22 (2004).
- [70] M. Methfessel and A.T. Paxton, High-precision sampling for Brillouin-zone integration in metals, Phys. Rev. B **40**, 3616–3621 (1989).
- [71] G. Makov and M. C. Payne, Periodic boundary conditions in *ab initio* calculations, Phys. Rev. B **51**, 074014 (1995).
- [72] Christoph Freysoldt, Jörg Neugebauer, and Chris G. Van de Walle, Fully *Ab Initio* Finite-Size Corrections for Charged-Defect Supercell Calculations, Phys. Rev. B **102**, 016402 (2009).
- [73] Christoph Freysoldt, Jörg Neugebauer, and Chris G. Van de Walle, Electrostatic interactions between charged defects in supercells, Phys. Stat. Solid. **248**, 1067 (2011).
- [74] Stephan Lany and Alex Zunger, Assessment of correction methods for the band-gap problem and for finite-size effects in supercell defect calculations: Case studies for ZnO and GaAs, Phys. Rev. B **78**, 235104 (2008).
- [75] Audrius Alkauskas, Peter Broqvist, and Alfredo Pasquarello, Defect Energy Levels in Density Functional Calculations: Alignment and Band Gap Problem, Phys. Rev. B **101**, 046404 (2008).
- [76] Hannu-Pekka Komsa, Peter Broqvist, and Alfredo Pasquarello, Alignment of defect levels and band edges through hybrid functionals: Effect of screening in the exchange term, Phys. Rev. B **81**, 205118 (2010).
- [77] Hannu-Pekka Komsa and Alfredo Pasquarello, Assessing

- the accuracy of hybrid functionals in the determination of defect levels: Application to the As antisite in GaAs, *Phys. Rev. B* **84**, 075207 (2011).
- [78] Audrius Alkauskas and Alfredo Pasquarello, Band-edge problem in the theoretical determination of defect energy levels: The O vacancy in ZnO as a benchmark case, *Phys. Rev. B* **84**, 125206 (2011).
- [79] Mao-Hua Du, Density Functional Calculations of Native Defects in $\text{CH}_3\text{NH}_3\text{PbI}_3$: Effects of Spin-Orbit Coupling and Self-Interaction Error, *J. Phys. Chem. Lett.* **6**, 1461–1466 (2015).
- [80] Ran He, Daniel Kraemer, Jun Mao, Lingping Zeng, Qing Jie, Yucheng Lan, Chunhua Lie, Jing Shuai, Hee Seok Kim, Yuan Liu, David Broido, Ching-Wu Chu, Gang Chen, and Zhifeng Ren, Achieving high power factor and output power density in *p*-type half-Heuslers $\text{Nb}_{1-x}\text{Ti}_x\text{FeSb}$, *Proc. Natl. Acad. Sci.* **113**, 13576–13581 (2016).
- [81] Joseph R. Sootsman, Huijun Kong, Ctirad Uher, Jonathan James D Angelo, Chun-I Wu, Timothy P. Hogan, Thierry Caillat, and Mercouri G. Kanatzidis, Large Enhancements in the Thermoelectric Power Factor of Bulk PbTe at High Temperature by Synergistic Nanostructuring, *Angew. Chem.* **47**, 8618–8622 (2008).
- [82] Y. Pei, S. Xiaoya, L. Aaron, L. Chen H. Wang, and G.J. Snyder, Convergence of electronic bands for high performance bulk thermoelectrics, *Nature* **473**, 66–69 (2011).
- [83] Y. Pei, H. Wang, and G.J. Snyder, Band engineering of thermoelectric materials, *Adv. Mater.* **24**, 6125–6135 (2012).
- [84] Kanishka Biswas, Jiaqing He, Ivan D. Blum, Chun-I Wu, Timothy P. Hogan, David N. Seidman and Vinayak P. Dravid, and Mercouri G. Kanatzidis, High-performance bulk thermoelectrics with all-scale hierarchical architectures, *Nature* **489**, 414–418 (2012).
- [85] G. E. Smith and R. Wolfe, Thermoelectric Properties of Bismuth- Antimony Alloys, *J. Appl. Phys.* **33**, 841–846 (1962).
- [86] G. S. Nolas, J. Sharp, and H. J. Goldsmid, *Thermoelectrics* (Springer, 2001).
- [87] F. Zhou, W. Nielson, Y. Xia, and V. Ozoliņš, Lattice Anharmonicity and Thermal Conductivity from Compressive Sensing of First-Principles Calculations, *Phys. Rev. Lett.* **113**, 185501 (2014).
- [88] Wu Li, Jesús Carrete, Nebil A. Katcho, and Natalio Mingo, ShengBTE: A solver of the Boltzmann transport equation for phonons, *Comput. Phys. Commun.* **185**, 1747–1758 (2014).
- [89] Alex Zunger, Beware of plausible predictions of fantasy materials, *Nature* **566**, 447–449 (2019).
- [90] Niculescu V, T. J. Burch, K. Rag, and J. Budnick, RMX Compounds Formed by Alkaline Earths, Europium and ytterbium - I. Ternary Phases with $M = \text{Cu, Ag, Au}$; $X = \text{Sb, Bi}$, *J. Less Common Met.* **166**, 319–327 (1990).